MNE 19 (2023) 100207

Contents lists available at ScienceDirect

Micro and Nano Engineering

journal homepage: www.sciencedirect.com/journal/micro-and-nano-engineering

Synthesis of plasmonic gold nanoparticles on soft materials for biomedical applications

Federica Granata [a,b], Noemi Pirillo [c], Alessandro Alabastri [d], Andrea Schirato [d,e,f], Luigi Bruno [g], Roberta Costa [c], Natalia Malara [h], Valentina Onesto [c], Maria Laura Coluccio [c], Mario Iodice [a], Giuseppe Coppola [a,*], Francesco Gentile [c,*]

[a] Institute of Applied Science and Intelligent System – CNR, via P. Castellino, 111, 80131 Napoli, Italy
[b] Mediterranea University of Reggio Calabria, Via dell'Università, 25, 89124 Reggio Calabria, RC, Italy
[c] Nanotechnology Research Center, Department of Experimental and Clinical Medicine, University "Magna Graecia" of Catanzaro, 88100 Catanzaro, Italy
[d] Department of Electrical and Computer Engineering, Rice University, Houston, TX 77005, USA
[e] Department of Physics, Politecnico di Milano, Piazza Leonardo da Vinci, 32, 20133 Milano, Italy
[f] Istituto Italiano di Tecnologia, via Morego 30, 16163 Genova, Italy
[g] Department of Mechanical Engineering, Energy Engineering and Management, University of Calabria, 87036 Rende, Italy
[h] Department of Health Sciences, University "Magna Graecia" of Catanzaro, 88100 Catanzaro, Italy

ARTICLE INFO

Keywords:
Soft materials
Nanoplasmonics
Metal-enhanced fluorescence
Electroless deposition
Immunoassay

ABSTRACT

Plasmonic metal nanomaterials are usually supported by rigid substrates, typically made of silicon or glass. Recently, there has been growing interest in developing soft plasmonic devices. Such devices are low weight, low cost, exhibit elevated flexibility and improved mechanical properties. Moreover, they maintain the features of conventional nano-optic structures, such as the ability to enhance the local electromagnetic field. On account of these characteristics, they show promise as efficient biosensors in biological, medical, and bio-engineering applications. Here, we demonstrate the fabrication of soft polydimethylsiloxane (PDMS) plasmonic devices. Using a combination of techniques, including electroless deposition, we patterned thin membranes of PDMS with arrays of gold nanoparticle clusters. Resulting devices show regular patterns of gold nanoparticles extending over several hundreds of microns and are moderately hydrophilic, with a contact angle of about 80°. At the nanoscale, scanning electron and atomic force microscopy of samples reveal an average particle size of ~50 nm. The nanoscopic size of the particles, along with their random distribution in a cluster, promotes the enhancement of electromagnetic fields, evidenced by numerical simulations and experiments. Mechanical characterization and the stress-strain relationship indicate that the device has a stiffness of 2.8 *MPa*. In biological immunoassay tests, the device correctly identified and detected anti-human immunoglobulins G (IgG) in solution with a concentration of 25 $\mu g/ml$.

1. Introduction

Plasmonic devices allow the generation, manipulation and enhancement of the electromagnetic (EM) field at optical frequencies at the metal-dielectric interface at the nanometer scale [1–3]. The confinement of EM fields caused by such structures improves the performance of spectroscopy, including fluorescence microscopy, and spectrometry techniques - where the EM radiation of a specified range of wavelengths interacts with a sample, changes its energy states and produces a measurable signal [1–3]. These amplification effects are at the origin of plasmon-enhanced detection techniques, such as surface-enhanced Raman scattering (SERS) spectroscopy [4–7] and metal-enhanced fluorescence (MEF) microscopy [8–10]. In light of the electromagnetic confinement effect they promote, many plasmonic nanostructured systems are used in biology, medicine and bio-engineering to analyze biological samples [11]. Plasmonic devices typically consist of gold or silver nanoparticles with different shapes and sizes in the low nanometer range, placed on planar rigid substrates, commonly made of, e.g., silicon or silicon dioxide. However, over the past few years the development of plasmonic metal nanostructures on soft materials has

* Corresponding authors.
E-mail addresses: giuseppe.coppola@cnr.it (G. Coppola), francesco.gentile@unicz.it (F. Gentile).

https://doi.org/10.1016/j.mne.2023.100207
Received 23 January 2023; Received in revised form 27 April 2023; Accepted 20 May 2023
Available online 23 May 2023
2590-0072/© 2023 Published by Elsevier B.V. This is an open access article under the CC BY license (http://creativecommons.org/licenses/by/4.0/).

gained momentum. This evolution of plasmonic devices offers advantages over traditional SERS/MEF substrates, such as low weight, low cost, high flexibility, and improved mechanical properties [12–15]. These characteristics enable unprecedented functions, including active optical tuning [16], wearable plasmonics for the detection of species at the biointerface [17], wearable healthcare devices [14], and strain sensing applications [18]. Following the classification proposed by Song and collaborators [14], existing methods to create soft nanoplasmonics substrates can be categorized as follows.

Physical blending and curing, in which metal nanoparticles are uniformly dispersed in the precursor using convenient physicochemical techniques [19–21]. *Template method*. In the method, the fabrication of soft nano-optics devices is assisted by an external template. The pattern is transferred from the template to a soft polymeric matrix through imprinting techniques, evaporation or sputtering techniques. Resulting motifs of nano-metal structures have the same macroscale size and shape of the originating template, and internal architecture at the nanoscale that is dependent on the parameters of the evaporation/sputtering process. Examples include cauliflower-like 3D Au NPs-PDMS composite film described in reference [22] and periodic wave-shaped microribbons array of Ag NPs and poly(ε-caprolactone) reported in reference [23]. *Embedded co-growth*. The method enables the fabrication of plasmonic nano-structures in which the metal nano-materials are intimately associated to the polymeric matrix, improving adhesion, enhancing stability, and reducing the physical and optical mismatch between the solid-polymeric phases in the device. This is achieved, as for an example, by thermal-radiation-assisted Au NPs encapsulation [24] or phase separation [25].

Examples of PDMS metal-nanoparticles functionalization, falling in the described categories, include a two-steps growth of AuNPs on PDMS, causing the formation of densely-packed 3D conglomerates of spheroids at the PDMS surface [26] and silver patterning on PDMS by inkjet printing [27]. In the above described methods plasmonic nanoparticles are either randomly dispersed within the soft polymeric substrate (*Physical blending and curing, Embedded co-growth*), or have characteristics limited by the geometry of the template and the parameters of evaporation/sputtering (*Template method*).

Here - in contrast to the methods of fabrication of soft plasmonic devices descrived above - we demonstrate the functionalization of soft polydimethylsiloxane (PDMS) membranes with gold nanoparticles clusters (Fig. 1a-c) using a combination of techniques, including site-selective electroless deposition [28,29].

Specifically, micrometric thick membranes were produced by standard spin coating and PDMS curing process. Then, micrometric OiR-resist micro-disks were transferred on the membranes by optical lithography, followed by amorphous-silicon deposition using plasma-enhanced chemical vapor deposition; the a-Si not directly interacting with the OiR micro-disks was removed by lift-off. As a final step, we deposited arrays of gold nanoparticles on a-Si patterns using electroless deposition, a method that enables the synthesis of metallic gold on an autocatalytic surface without externally applied voltages [30]. In tests in which the device was functionalized with human immunoglobulins G (IgG), we demonstrated the recognition, capture and amplification of anti-human IgG with a concentration of 25 $\mu g/ml$, with high reproducibility and reliability. The sensor device we propose can be used in medicine, biology and biotechnology for the detection of analytes and biomarkers in a low concentration range, the diagnosis and prognosis of pathologies, or the assessment of the physiological conditions of patients and individuals.

2. Methods

2.1. Fabrication of micro-patterned PDMS membranes

The fabrication of plasmonic devices on a thin polydimethylsiloxane (PDMS) membrane involves several technological steps summarized in the Fig. 2. (100) silicon wafers with resistivity $1 - 5$ Ohm/cm were treated by deep cleaning with acetone and isopropanol in a sonicator (Fig. 2a). The substrates were then treated with an oxygen plasma ($RF\ power = 100W$, $O_2\ flow = 100\ sccm$, $t = 5min$) to hydrophilicize the surface and ensure uniform coverage of the PDMS layer. A 10 : 1 mixture of PDMS and cross-linking agent (Sylgard) were poured onto the silicon

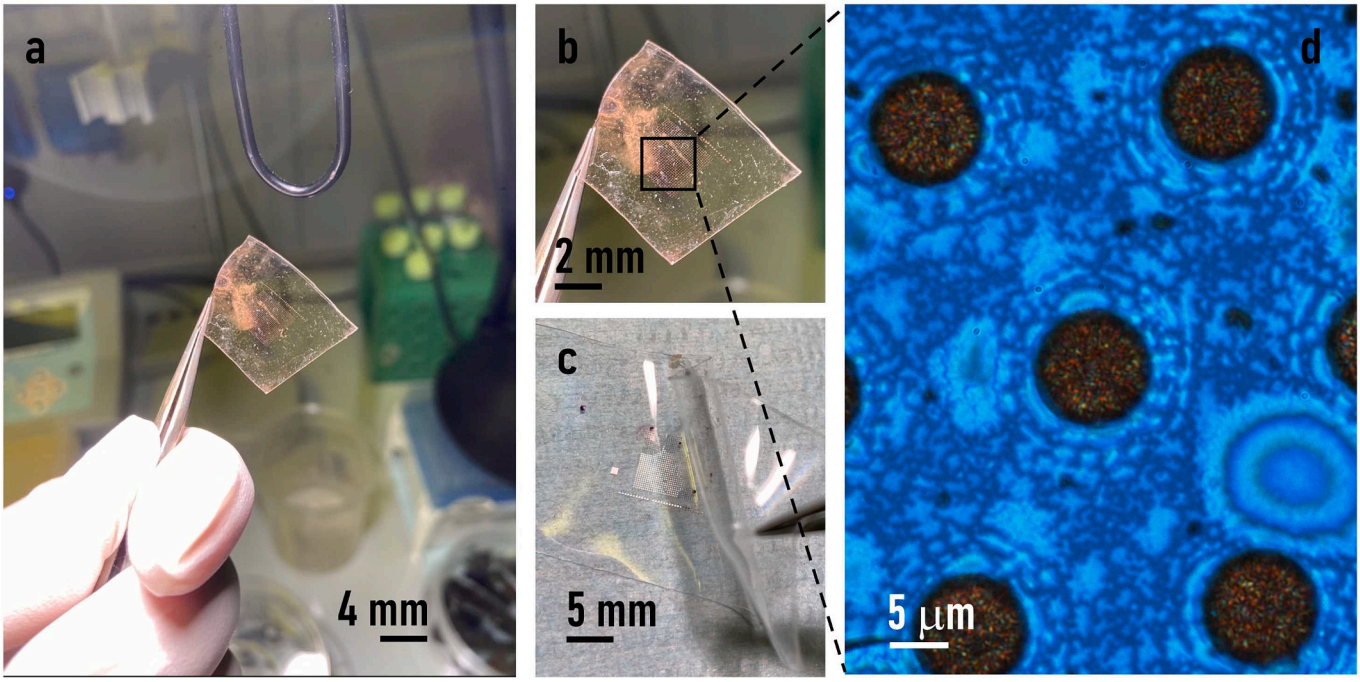

Fig. 1. Images of soft PDMS membranes decorated with patterns of gold nanoparticle clusters. Due to the very low value of elasticity and bending stiffness, the devices deform under their own weight (a-c). Optical image of the clusters of gold nanoparticles (d). (For interpretation of the references to colour in this figure legend, the reader is referred to the web version of this article.)

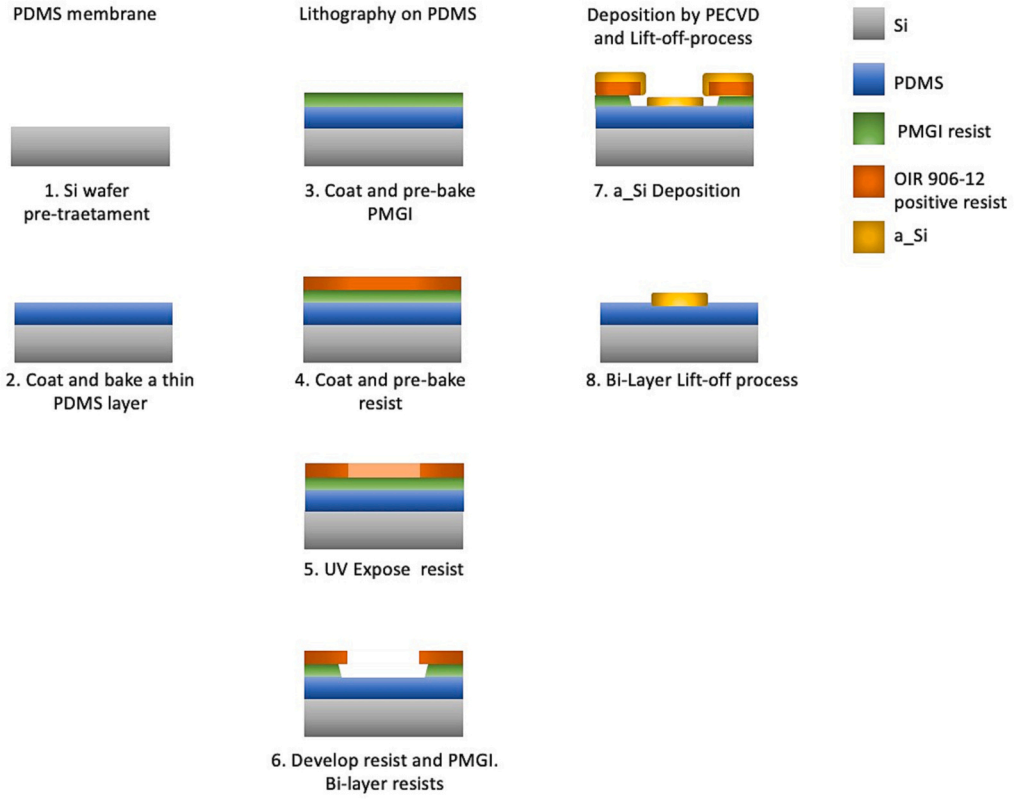

Fig. 2. Schematics of the fabrication process of micrometric amorphous silicon patterns on thin PDMS membranes. Silicon wafers were cleaned for subsequent frabrication-steps (a). One layer of PDMS was deposited on the Silicon surface (b). The PMGI photoresist, characterized by a high dissolution property, was spun on the PDMS surface (c). The positive resist OIR 906–12 was, in turn, spun on the PMGI surface (d). The positive photoresist was then patterned with arrays of micrometric disks using optical lithography (e-f). Following surface patterning, amorphous silicon (a-Si) was deposited on the samples (g). Finally, to remove the a-Si from the area outside the array of disks, samples were immersed in acetone at 60 ° *C* and sonicated for 15 minutes (h).

wafers and spun at 1000 *rpm* for 60 *s* to obtain a 200 μm thick PDMS membrane, that was subsequently polymerized for 30 minutes at 100 ° *C* (Fig. 2b). The surface of the PDMS membranes were then patterned with regular arrays of micrometric polymeric disks, with a diameter of 10 μm. To optimize the successive lift-off step, we deposited a double layer of photosensitive PMGI and OIR 906–12 material in the optical lithography process. The PMGI photoresist, characterized by a high dissolution property, was spun at 4000 *rpm* for 60 *s* on the wafer and pre-baked at 150 ° *C* for 5 minutes (Fig. 2c). Then, the positive resist OIR 906–12 was spun at 4000 *rpm* for 60 *s*, and baked at 95 ° *C* for 60 *s* (Fig. 2d). The layers were then exposed to UV light with an energy density of 140 mJ/cm^2 for 14 *s* to transfer the pattern design from the mask to the sample, followed by post bake of sample at 120 ° *C* for 60 *s* (Fig. 2e). Samples were then developed using OPD 4262 for 60 *s* and rinsed with deionized water (Fig. 2f). Following surface patterning, amorphous silicon (a-Si) was deposited on the samples. The deposition of a 160 *nm* thick layer of a-Si was performed by plasma-enhanced chemical vapor deposition (PECVD) using the following values of the process parameters: pressure $P = 1.2$ *mbar*, temperature $T = 100$ ° *C*, *Power* $= 2W$, flow of $SiH_4 = 600$ *sccm*, *deposition time* $= 5$ *min* (Fig. 2g). Finally, to remove the a-Si from the area outside the array of disks, samples were immersed in acetone at 60 ° *C* and sonicated for 15 minutes (Fig. 2 h).

Further to this point. PECVD is a deposition process that uses gaseous precursors and glow-discharge plasmas supported in a vacuum chamber to simultaneously activate vapor phase chemical reactions and film deposition. Specifically, a polarizing voltage is applied to the substrate material to attract ionized species to the substrate surface. The main advantage of the technique is that the deposition process takes place at low temperatures (typically from near room temperature to around 350 ° *C*), allowing soft materials (such as the PDMS) to be used as substrates. In addition, the uniformity, adhesion and mechanical integrity of the deposited material can be controlled by regulating the parameters of the plasma process (such as the operating pressure and flow rate of the precursor gases, the power input to the plasma discharge and the polarization on the substrate).

2.2. Electroless deposition of gold nanoparticles clusters

To accomplish the deposition of gold nanoparticles on the surface of a-Si micro-patterned on the PDMS membranes, we used electroless deposition. Such a method allows reduction of ions into metallic gold on the autocatalytic surface of silicon [8]. We placed the PDMS membranes in contact with a 0.15 *M* solution of hydrofluoric acid (HF) and gold chloride ($AuCl_3$) at a concentration of $C = 5$ *mM*, for 40 min. The temperature of the system was maintained at $T = 50$ ° *C*, for the whole duration of the process. Hydrofluoric acid and gold chloride were purchased from Merck. Since electroless deposition is a stochastic mechanism of growth, individual particle synthetized through this methods are roughly semi-spherical, as evidenced by previous experimental and theoretical reports [30].

2.3. SEM characterization

Morphological characterization of soft plasmonic devices has been carried out by scanning electron microscopy (SEM). SEM images of the samples were captured using a Sigma 300VP (Zeiss, Germany) system. During the acquisitions, an accelerating voltage of 3 kV was used. More than 10 SEM images were acquired for each sample morphology.

2.4. AFM characterization

Atomic force microscopy (Park XE-70) was used for examining the nanoscale topography of the samples. All the measurements were performed in intermittent contact mode in a dry environment over a region of 8 $\mu m \times 8$ μm. Room temperature was held fixed for all the acquisitions. Ultra-sharp silicon probes with a nominal tip radius of less than 10 *nm* were used to achieve high resolution. Multiple measurements were done in different scan directions to avoid artifacts. At least four images

in height mode were recorded per sample. The images were acquired at a scanning rate of 0.5 *Hz* with a resolution of 256 × 256 points. Images were then post-processed to extract the average particle size, the average and root square mean values of roughness, and the fractal dimension of the samples. While the resolution we have used for the AFM imaging of the device is not ultra-high, still it allows to describe with a sufficient level of detail the topography of the clusters of gold-nanoparticles on the device. This is evidenced from the top-view of the AFM image of the same profile taken with similar resolution and pixel size – where individual gold nanoparticles are easily detected and separated from the background (Supporting Information Fig. S1). Convenient post processing of the image using interpolation methods, such as sub-pixel accuracy edge fitting, are then used to determine the values of roughness, average particle size, and fractal dimension, with good accuracy.

SEM and AFM characterization of sample surfaces has been carried out on PDMS membranes detached from the silicon support and then repositioned on standard sampler-holder. To assess the morphology of the soft-plasmonic device in unconstrained conditions - i.e. with the PDMS membrane left free to bend, deform, reshape, and readapt to external surfaces and interfaces. The PDMS coating layer was peeled out from the silicon support by hand with the aid of clean-room tweezers.

2.5. Deriving the fractal dimension of the samples

The topography of the gold nanoparticle clusters was processed using the methods described in reference [31]. The power spectrum density function (PS), derived for each AFM image, shows a linear behaviour in a log-log plot. The derivative of the spectrum with respect to the space frequency (β), is related to the fractal dimension D_f of a surface as $D_f = (8 - \beta)/2$.

2.6. Mechanical characterization of PDMS membranes

We have performed mechanical characterization of samples to understand what is the value of elasticity of similar soft PDMS plasmonic devices that can be obtained by standard polymerization methods. The elasticity or stiffness of soft devices is important in future possible applications, where the device will be integrated in tissues and organs for direct recording of electro-physiological signals of cells. In similar applications, the lower the mechanical, chemical, and electrical mismatch between the device and the tissue, the higher the quality of the measurement and the performance of the device. Fabrication processes and tools are likely to improve the current analysis and sensing practice of biological solutions, cells or molecules, if they address the discrepancies between the biotic and abiotic system [32]. The mechanical characterization method was based on the procedure adopted in reference [33]. The schematic of the experimental setup is shown in the Supporting Information Fig. S2. The tensile test was applied to a thin layer specimen by the universal testing machine MTS model Criterion 42, consisting of a single column tabletop-framed electromechanical testing system equipped for this specific application with the load cell LSB.102 (load capacity 100 *N*, class 0.5 from 1% to 100% of load capacity). The load was applied by manual vice action grips for testing paper, plastic film, textiles, sheet materials and packaging components. Tests were carried out in displacement control mode by setting the crosshead speed to 2 mm/min. Tests end with the failure of the specimen or when the length of the specimen is about doubled, whichever event occurs before. Voltages proportional to the load and displacement values were used as reference signals to synchronize the images acquired by the camera, a Prosilica model ATV-GT2450 (resolution 2448 × 2050 pixel, pixel dimension 3.45 μm × 3.45 μm, maximum frame rate 15 *Hz*). The image illumination was optimized by two diode light sources placed symmetrically around the camera. All the signals (voltages and images) were acquired by a workstation interfaced with all devices using the data acquisition system, ISI-SYS model DAQ-STD-8D. 2D-DIC method was used to evaluate the longitudinal strain gradient. A region of interest of about 3 *mm* × 3 *mm* far from the clamping area and from the edges of the specimen was studied, using a subset of 21 × 21 pixels and a step of 5 pixels in both horizontal and vertical directions. Considering the magnification ratio (6.25 μm/pixel), the two displacement components were evaluated on about 13000 points. The strain was evaluated by fitting the displacement field with bilinear functions.

2.7. Surface functionalization

Soft PDMS plasmonic substrates were functionalized with human IgG antibodies and then incubated with FITC-labelled anti-human IgG antibodies to demonstrate antibody-antigen identification and capture, and verify the amplification effects of the device. To accomplish functionalization, plasmonic devices were washed with 200 μl of MilliQ deionized water and dried with nitrogen. Then, samples were incubated with 20 μl of human IgG antibodies (Thermo Fisher Scientific) for 20 min. After removal of the excess antibodies, samples were washed with 200 μl PBS (Merck) once and 200 μl of MilliQ deionized water twice. Molecular binding of the antibody-antigen complex was carried out by dropping 20 μl of the solution of FITC-labelled anti-human IgG antibodies (Thermo Fisher Scientific) on surfaces. The drop was left to adsorb for 20 min, then samples were washed with 200 μl PBS twice and 200 μl of MilliQ deionized water three times. In these assays, the concentration of human and anti-human IgG antibodies was of 25 $\mu g/\mu l$.

2.8. Fluorescence microscopy of samples

Fluorescence images of samples were recorded employing a Nikon Eclipse Ti inverted microscope equipped with 10× (*NA* 0.45) and 30× (*NA* 0.5) objectives. To investigate the binding of human anti-human-FITC IgG, the system was excited with an Ar^+ laser at 488 *nm*, and the emission bandwidth was from 520 to 600 nm. All the images were collected at 12-bit colour depth with a resolution of 1024 × 1024 pixels, using an integration time of 2 *s*.

2.9. Simulating EM fields around NPs clusters

To corroborate the experimental observations, measurements have been combined with a numerical analysis of the electromagnetic response of the Au NP cluster. A finite element method (FEM) based model has been developed using commercial software (COMSOL Multiphysics, version 5.6). The numerical calculation solves Maxwell's equation in the frequency domain to determine the electric field everywhere across the simulated geometry, consisting of the layer of clustered Au NPs on a 100 − *nm* a-Si film. The structure lies on a PDMS substrate (treated as semi-infinite) and is surrounded by air. In order to accurately model the behaviour of the Au aggregate, the corresponding numerical domain is built based on the actual morphology of the experimental structure. In particular, the atomic force microscopy (AFM) profile (i.e., a collection of height values as a function of the in-plane coordinates spanning an area of 2 μm × 2 μm) of the sample was measured, imported in the software and directly employed to define (employing the parametric surface built-in option) a numerical surface. To limit the computational effort, a subset of the measured heights (corresponding to a 500 *nm* × 500 *nm* area) was used and assumed to repeat periodically in the (*xy*)-plane. Given the randomicity of the experimental cluster AFM profile, this approximation is expected to have a minor impact on the overall optical response of the structure. Note that the (2 μm × 2 μm) Au surface shown in Fig. 4d has been obtained by mirroring in post-processing the domain used in the simulations for better visualising the results. The model assumes a monochromatic plane wave excitation at $\lambda = 491$ *nm*, linearly polarized along the *x*-direction and impinging from the air side at normal incidence. Gold permittivity has been defined according to reference [34], a-Si complex-valued refractive index has been taken from reference [35], while PDMS (air) refractive index was set equal to 1.43. User-

defined port boundary conditions (BCs) were defined to model the electromagnetic excitation, while perfect electric and magnetic conductor BCs were employed to mimic the in-plane periodicity of the structures. Finally, perfectly matched layers (PMLs) were defined at the top and bottom of the domain (behind the input and output ports) to avoid spurious reflections in the modelled domain. Due to the peculiar morphology of the Au surface, a maximum element size equal to 20 *nm* and $\lambda/10$ was used to mesh the area surrounding the Au NP cluster and the remaining domains, respectively.

3. Results

3.1. Generating soft PDMS plasmonic devices

We used standard optical imaging and SEM (Methods) to assess the fabrication process capability to generate arrays of Au nanoparticle clusters on soft PDMS membranes. Bright-field optical images and low-magnification SEM micrographs of the devices (Fig. 1d, Figs. 3a-b) show the remarkable spatial extent of the structures, which are uniformly distributed over large areas up to several hundred square micrometers. In these regions, the clusters have a circular shape and hexagonal packing, with a diameter of 10 μm and lattice constant, i.e. distance between unit cells of 30 μm. High magnification SEM micrographs of the device (Figs. 3c, Supporting Information Fig. S3) illustrate the random, non-periodic arrangement of the gold nanoparticles within each cluster, with an average particle size of ~50 *nm* and small variations around the mean. The SEM micrograph in Fig. 3c has a sufficiently high level of detail to show the irregular, rough surface of the PDMS substrate underneath. In the image, the ridges and ripples are traits characteristic of soft materials that can slightly deform following fabrication.

3.2. Examining the morphology of the devices at the nanoscale

We used AFM (Methods) to examine the geometrical characteristics of the device at the nanoscale. The AFM image of the sample surface over a region of interest of 8 $\mu m \times 8\ \mu m$ is shown in Fig. 4a. Post processing analysis of AFM data enabled to determine the average (R_A) and root mean square (R_{rms}) values of roughness of the plasmonic Au nanoscale substrate as R_A~16 *nm* and R_{rms}~20 *nm*, respectively. In a separate Supporting Information Table S4, we show how the roughness of gold nanoparticles clusters compares to the values of roughness determined for naked PDMS and amorphous silicon.

Distribution of profile heights (Fig. 4b) illustrates that the particle size ranges over an interval of length 100 *nm*, with a mean value of 50 *nm*, consistent with the SEM observations. AFM topography profiles of the nanograins were then Fourier-transformed and processed using the methods reported in reference [31] to obtain the characteristic power spectrum (PS) of the surface (Fig. 4c). The PS illustrates how the structure of a surface changes as a function of scale. Approximately horizontal PS diagrams are indicative of self-affine surfaces, where the information content of the image varies moderately with space frequency q. Thus, for a surface, the slope (β) of the PS and the fractal dimension (D_f) are linked through the relationship $D_f = (8 - \beta)/2$. For this configuration, the fractal dimension was determined as D_f~2.4.

3.3. Optical properties of soft plasmonic devices

In terms of the optical behaviour of the system, the values of surface roughness, size distribution, and fractal dimension derived for the considered plasmonic substrate give rise to confinement effects of the EM field at the metal-air interface, where asperities of the metal surface spatially localize the electromagnetic radiation. We performed numerical simulations to solve the Maxwell's equation and determine the EM distribution at the nanostructured metal surface (see Methods section 2.9). To achieve maximum precision and accuracy, we modelled the geometry of the plasmonic surface after the topography of the real physical prototype by importing into the simulation software the experimental AFM profile. Upon excitation with a linearly polarized plane wave at 491 *nm*, we then computed the EM field enhancement squared, $(E/E_o)^2$, with E and E_o the amplitudes of the local induced and impinging EM fields respectively. Results of the analysis (Figs. 4d-e) indicate that the EM field intensity is enhanced by a factor of ~10 on the

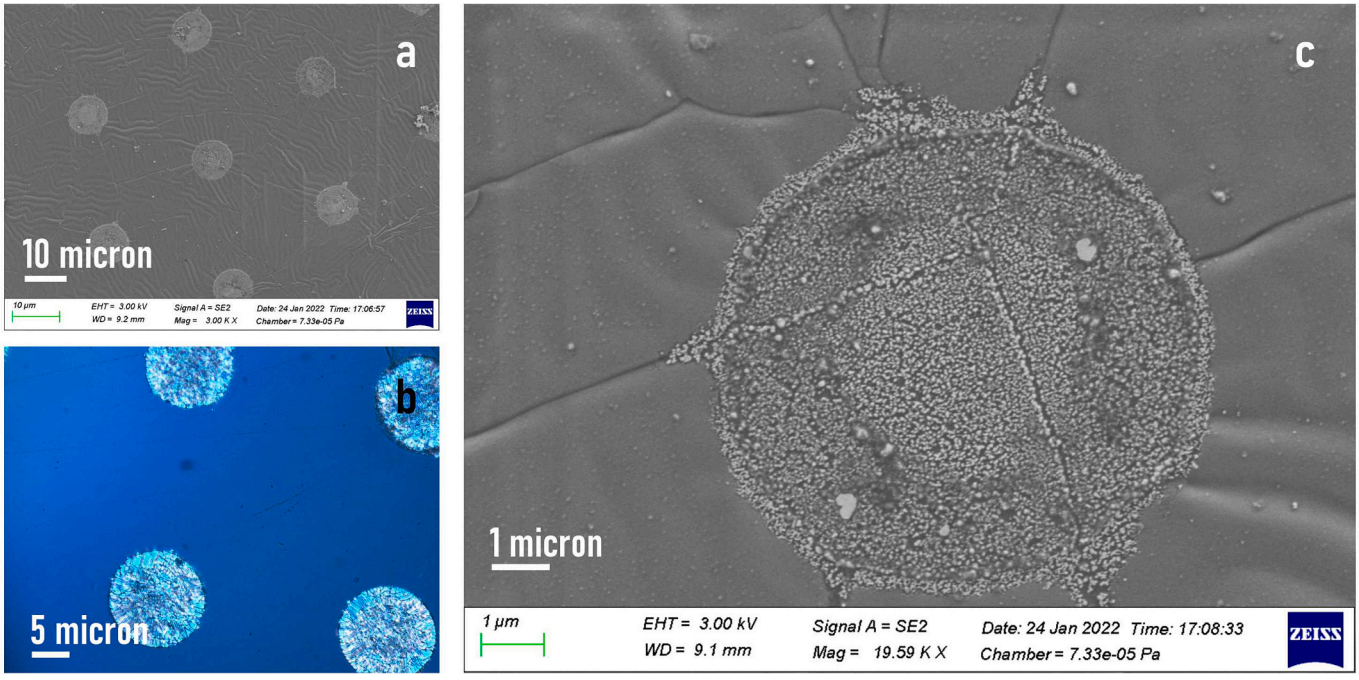

Fig. 3. Scanning electron microscopy (SEM) micrographs (a) and optical images (b) of the surface of the PDMS plasmonic devices taken at low magnification. The images show the periodic array of discoidal nanoparticle clusters covering the sensor surface. SEM micrograph the surface of the PDMS plasmonic device taken at higher magnification (c). The micrograph illustrates the size, shape characteristics and morphology of the gold nanoparticles in a cluster. (For interpretation of the references to colour in this figure legend, the reader is referred to the web version of this article.)

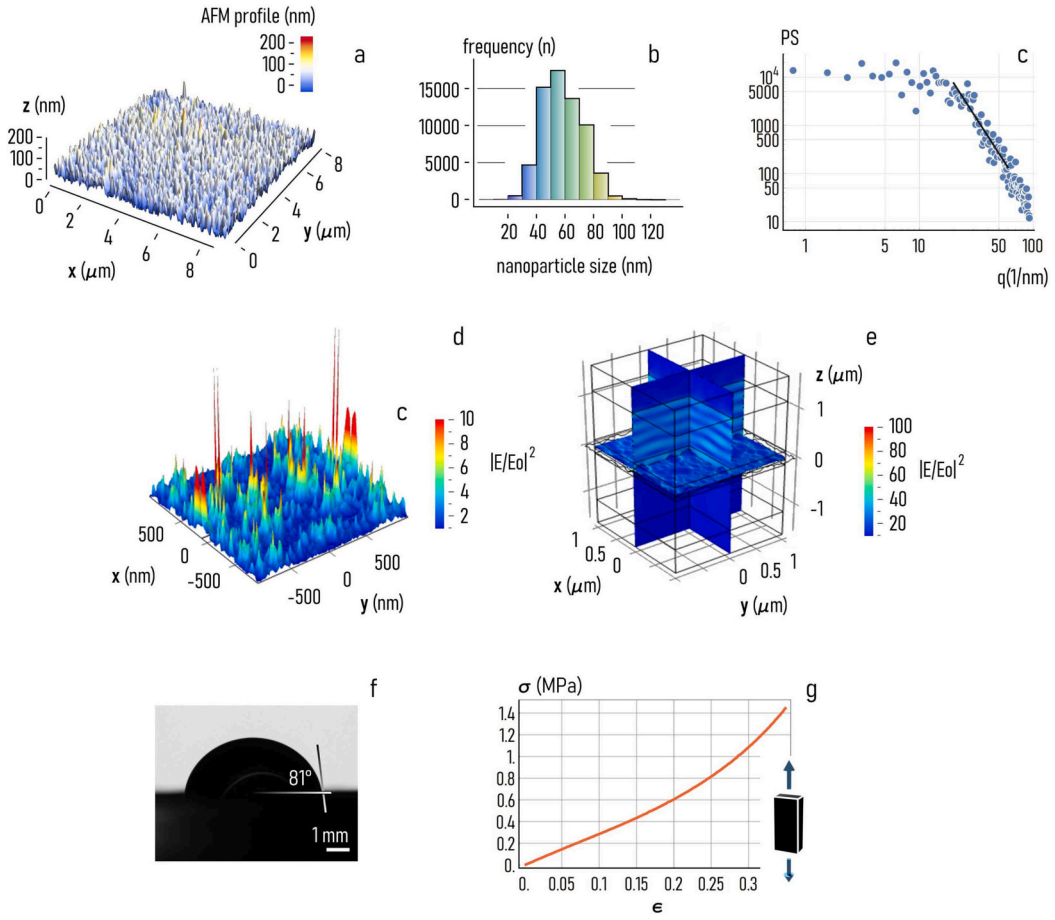

Fig. 4. Atomic force microscopy (AFM) profile of the gold nanoparticles measured on the surface of the soft plasmonic device (a). Height profile distribution of nanoparticles (b). Power spectrum density function relative to the AFM image in (*a*) (c). Height impression of the electromagnetic field enhancement simulated at the surface of the gold nanoparticles cluster (d). Density plot of the electromagnetic field enhancement simulated in the space above the surface of the gold nanoparticles cluster (e). Contact angle of a microliter drop of DI water with the PDMS plasmonic surface (f). Stress strain curve of the PDMS device (g). (For interpretation of the references to colour in this figure legend, the reader is referred to the web version of this article.)

surface of the device and by a factor ~100 in the region *above* the plasmonic device – the maximum EM enhancement is found in a position elevated from the surface of gold nanoparticles of approximately 80 *nm*. This evidenced from the plot of the maximum EM squared enhancement in a plane positioned at *z nm* from the nano-scale active surface, as a function of *z* (Supporting Information Fig. S5). Since the enhancement factor $(E/E_o)^2$ investigated is proportional to the fluorescence signal emitted from molecules adsorbed to the nanoscale surface, simulations also indicate that the device can be used efficiently for the diagnosis of biomarkers or species of biomedical interest. Futher to the end to characterize the optical properties of the devices, we have measured the absorbance of the sensor as a function of the wavelength (Supporting Information Fig. S6). Results indicate that the absorbance peak is at centered around, approximately, 550 *nm*. The values of absorbance vary from 45% to 65%. Remarkably, the measured range of absorbance is consistent with the amplification of the fluorescence-signal in the 520 – 600 *nm* interval.

3.4. Mechanical characteristics of soft plasmonic devices

We performed additional tests to verify the chemical and mechanical characteristics of the device. The wetting characteristics of the PDMS sample surface were determined using an automatic contact angle meter, measuring the water contact angle of one drop of deionized water at room temperature. Measurements indicate that the device is moderately hydrophilic, exhibiting a contact angle of about 81° (Fig. 4f). Mechanical characterization and the stress-strain curves of PDMS membranes, determined through an elongation test and digital image correlation as described in methods, indicate that the device has an estimated stiffness of E~2.8 MPa (Fig. 4g), still larger than Young's modulus of tissues and organs (E~10 – 1000 *kPa*) [36,37], but lower than the elasticity of typical engineering materials, such as metals, ceramics, and composites.

3.5. Soft plasmonic devices as bio-sensors

To demonstrate the analytical capability of the device, we adsorbed on the surface of gold nanoparticle clusters human immunoglobulins G (IgG) (Methods). Upon functionalization with IgG, we challenged the sensor device with a solution of anti-human IgG, i.e. the target molecule, conjugated with bright green FITC fluorescence (Fig. 5a). This antibody-antigen immobilization scheme was verified using fluorescence microscopy. Fluorescence images of the sensor device (Fig. 5b, c) show the high intensity and good colocalization of the fluorescence signal with the plasmonic active sites of the device - demonstrating selective capture and identification of the biological marker in solution. Additional images relative to sample repeats of the same experiment are reported in a separate Supporting Information Fig. S7.

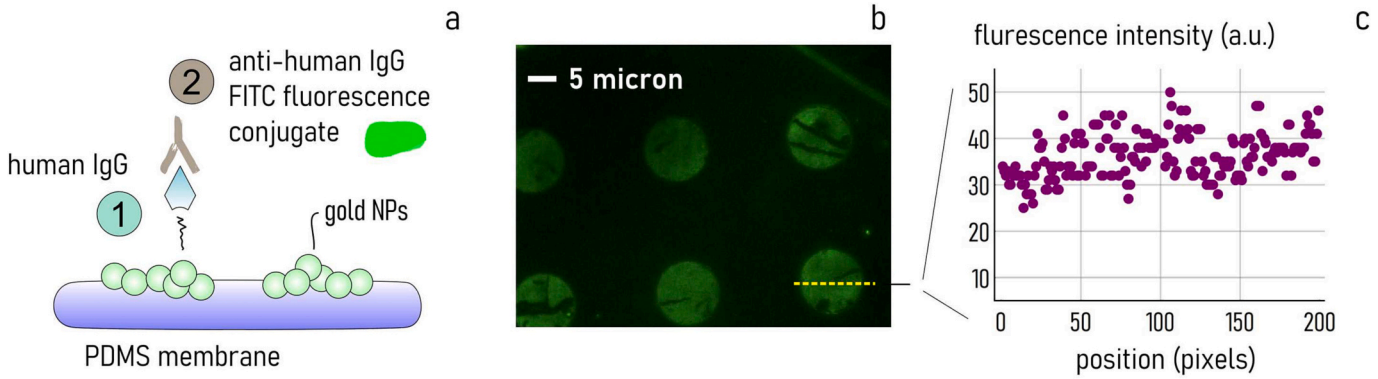

Fig. 5. Scheme of the antigen-antibody immunoassay test performed by the sensor device (a). Upon functionalization with humang IgG, and exposure to anti-human IgG, the sensor device correctly captured anti-human IgG in solution, evidenced by bright green fluorescence of samples (b). Fluorescence intensity profile measured across a cluster of gold-nanoparticles after incubation with anti-human IgG (c). (For interpretation of the references to colour in this figure legend, the reader is referred to the web version of this article.)

3.6. Verifying site-selective amplification of fluorescence signal by gold nano-particles

Specific, site-selective functionalization of plasmonic nano-structures by human IgG was achieved because of the physical and chemical characteristics of gold nanoparticles (NPs) on the surface. Because of a high surface energy density, gold NPs strongly associate with blood biomolecules and proteins [38,39], including immunoglobulins [40], with a binding constant as high as $10^{-9}\ M^{-1}\ s^{-1}$. To verify that the functionalization of human IgGs is specific to the nano-metals, we have performed an additional test campaign where gold NPs were deposited on flat silicon substrates. Then, samples were functionalized with human IgGs using the methods described in the paper, and challenged with a solution containing anti-human IgGs. Post processing of fluorescence images acquired on nanostructured surfaces (Supporting Information 8) illustrates that the relative intensity of the signal is ~1 arbitrary units (i) within the clusters of gold nanoparticles, and is ~0.04 arbitrary units (ii) on flat silicon, with a consequent fluorescence enhancement factor of about ~20, a value consistent with theoretical predictions and finite element simulations of the EM field.

The experiments reported in the SI 7 were aimed at quantifying the enhancement of the fluorescence signal on the device, compared to unstructured silicon. To understand whether the clusters of gold nanoparticles perform better than a continuous, nominally flat gold surface we did perform additional experiments (Supporting Information 9). In these experiments, two different sensor surfaces, i.e. a nominally flat gold on silicon and clustered gold nanoparticles on PDMS, were challenged with a bright green FITC fluorescence molecule with a concentration of 100 *μg/ml*. Sample surfaces were left in contact with the fluorescence solution for 10 min, gently washed with D.I. water and dried under nitrogen flux. Samples were then imaged using fluorescence microscopy using the settings reported in the methods of the paper. After acquisition and convenient post-processing of images, intensity values of samples were reported as a function of sample type. Results indicate that the average fluorescence intensity measured on the nano-patterned gold surface is ~3 times higher than the signal measured on flat silicon surface. Thus, a nano-scale gold substrate improves over a smooth gold surface in terms of fluorescence intensity of some 3 folds.

3.7. Verifying selectivity and specificity of the sensor device

Moreover, to substantiate the claim of selectivity and specificity that we have made in the manuscript, we have performed additional experiments in which we have functionalized the PDMS sensor device with human immune-globulins G (h-IgG), i.e. the ligand molecule. Then, we challenged the device with artificial complex mixtures containing goat anti-human IgG (g-Ah-IgG), i.e. the target molecule, a bright green FITC fluorescence conjugate that binds to g-Ah-IgG, and a number of competing interferents that can prevent the correct recognition and measure of Ah-IgG (Supporting Information 10). We used two different inteferents. In a first test, we used bovine serum albumin (BSA), that is a globular protein with high molecular weight, i.e. 60 *kDa*. In a second test, we used rabbit anti-goat IgG (r-Ag-IgG) as an antagonist of anti-human IgG. r-Ag-IgG has a significant affinity for h-IgG. Thus, in these competing assays, the mechanisms of interference are different. While BSA can possibly hamper (h-IgG)-(g-Ah-IgG) complexation because of steric hindrance, r-Ag-IgG can potentially hinder the correct functioning of the device because of direct specific coupling to h-IgG, replacing partially or totally g-Ah-IgG.

Results of the tests, reported in a separate Supporting Information 10, show that even in the presence of competing molecules, g-Ah-IgG is recognized and secured to the sensor device surface efficiently. Quantitative analysis of data also indicates that the selectivity of the device is of about 81% when considering weak antagonists of adhesion (BSA), and of about 49% when considering strong antagonists of adhesion (r-Ag-IgG). In comparison, in the case of non-specific binding (i.e. incubation of fluorescent g-Ah-IgG with a non-functionalized device) the value of selectivity has been assessed as ~40%. Figures and percentages have been calculated relative to the human-anti-human IgG complexation without interferents.

4. Discussion and conclusions

We have developed a method to decorate soft PDMS materials with clusters of gold nanoparticles. The shape and size of the nanoparticles in each cluster can possibly generate plasmonic effects, that in turn amplify the spectroscopy and fluorescence signal of biological markers anchored to the nanomaterial structure. In experiments in which the device was functionalized with human immunoglobulins (IgG) and exposed to anti-human IgG, we demonstrated antigen-antibody recognition by fluorescence microscopy.

Differently from other existing techniques of fabrication of soft plasmonic devices, described in the Introduction, the method that we have used in this study attains maximum control over the shape and size of metal nanostructures on PDMS. This is achieved by combining different techniques: (i) optical/electron lithography, (ii) silicon PECVD deposition, and (iii) electroless growth. While lithography and deposition techniques define with high precision the pattern on the substrate where nanoparticles can be positioned, electroless growth enables nanoparticle deposition, growth, and localization with nanometric precision [28,41].

The technique described in this study and its more sophisticated

evolutions that will be developed over time can thus improve over other existing methods of fabrication in terms of dimensional control and precision of the plasmonic nano-structures. Remarkably, the method is amenable to scale-up enabling the fabrication of nano-scale devices over millimeter to centimeter areas.

Moreove, since PDMS is biocompatible and biostable, with a stiffness of about 2.8 *MPa*, the plasmonic device that we have produced can possibly be implanted in tissues or organs for localized, site-selective sensing of biomolecules.

Declaration of Competing Interest

Francesco Gentile reports financial support was provided by Italian Association for Cancer Research. Francesco Gentile reports a relationship with Magna Graecia University of Catanzaro that includes: employment and non-financial support.

Data availability

Data will be made available on request.

Acknowledgements

This study was partially funded by the Italian Association for Cancer Research (AIRC) under the grant number AIRC IG 2021 ID 25656 and by the European Union - NextGenerationEU (National Sustainable Mobility Center CN00000023, Italian Ministry of University and Research Decree n. 1033 - 17/06/2022, Spoke 11 - Innovative Materials & Lightweighting). A.S. acknowledges support from the METAFAST project that received funding from the European Union Horizon 2020 Research and Innovation programme under Grant Agreement No. 899673. The opinions expressed are those of the authors only and should not be considered as representative of the European Union or the European Commission's official position. Neither the European Union nor the European Commission can be held responsible for them.

References

[1] M. Bauch, K. Toma, M. Toma, Q. Zhang, J. Dostalek, Plasmon-enhanced fluorescence biosensors: a review, Plasmonics 9 (2014) 781–799.
[2] A.G. Brolo, Plasmonics for future biosensors, Nat. Photonics 6 (2012) 709–714.
[3] P. Strobbia, E. Languirand, B.M. Cullum, Recent advances in Plasmonic nanostructures for sensing: a review, Opt. Eng. 54 (2015), 100902.
[4] J. Kneipp, H. Kneipp, K. Kneipp, SERS-a single-molecule and nanoscale tool for bioanalytics, Chem. Soc. Rev. 37 (2008) 1052–1060.
[5] K. Kneipp, Surface-enhanced Raman scattering, Phys. Today 60 (2007) 40–47.
[6] K. Kneipp, H. Kneipp, S. Abdali, R. Berg, H. Bohr, Single molecule Raman detection of Enkephalin on silver colloidal particles, Spectroscopy 18 (2004) 433–440.
[7] K. Kneipp, Y. Wang, H. Kneipp, L.T. Perelman, I. Itzkan, R.R. Dasari, M.S. Feld, Single molecule detection using surface-enhanced Raman scattering (SERS), Phys. Rev. Lett. 78 (1997) 1667–1670.
[8] E. Battista, M.-L. Coluccio, A. Alabastri, M. Barberio, F. Causa, P.-A. Netti, E. Di Fabrizio, F. Gentile, Metal enhanced fluorescence on super-hydrophobic clusters of gold nanoparticles, Microelectron. Eng. 175 (2017) 7–11.
[9] W. Deng, F. Xie, H.T.M.C.M. Baltarac, E.M. Goldys, Metal-enhanced fluorescence in the life sciences: here, now and beyond, Phys. Chem. Chem. Phys. 15 (2013) 15695–15708.
[10] K. Ray, J.R. Lakowicz, Metal-enhanced fluorescence lifetime imaging and spectroscopy on a modified SERS substrate, J. Phys. Chem. C 117 (2013) 15790–15797.
[11] A. Minopoli, B. Della Ventura, B. Lenyk, F. Gentile, J.A. Tanner, A. Offenhäusser, D. Mayer, R. Velotta, Ultrasensitive antibody-aptamer plasmonic biosensor for malaria biomarker detection in whole blood, Nat. Commun. 11 (2020) 1–10.
[12] A. Gontier, J. Marae-Djouda, A. Hmima, J. Proust, N.-B. Bercu, L. Le Joncour, S. Stagon, G. Konoplev, S.-A. Tarasov, P.-M. Adam, J. Gardan, B. Panicaud, M. Molinari, T. Maurer, Flexible plasmonic and strain sensors: fabrication, design and perspectives, IOP Conf. Series: J. Phys. 1461 (2020), 012096.
[13] S. Kumari, S. Mohapatra, R.S. Moirangthem, Development of flexible Plasmonic sensor based on imprinted nanostructure array on plastics, Mater. Today: Proceed. 5 (2018) 2216–2221.
[14] L. Song, J. Chen, B.B. Xu, Y. Huang, Flexible plasmonic biosensors for healthcare monitoring: progress and prospects, ACS Nano 15 (2021) 18822–18847.
[15] S. Torino, L. Conte, M. Iodice, G. Coppola, R.D. Prien, PDMS membranes as sensing element in optical sensors for gas detection in water, Sens. Bio-Sens. Res. 16 (2017) 74–78.
[16] J. Peng, H.-H. Jeong, M. Smith, R. Chikkaraddy, Q. Lin, H.-L. Liang, M.-F.-L. De Volder, S. Vignolini, S. Kar-Narayan, J.J. Baumberg, Fullyprinted flexible plasmonic metafilms with directional color dynamics, Adv. Sci. 8 (2021) 2002419.
[17] Y. Wang, C. Zhao, J. Wang, X. Luo, L. Xie, S. Zhan, J. Kim, X. Wang, X. Liu, Y. Ying, Wearable plasmonic-metasurface sensor for noninvasive and universal molecular fingerprint detection on biointerfaces, Sci. Adv. 7 (2021) eabe4553.
[18] P. Jia, D. Kong, H. Ebendorff-Heidepriem, Flexible plasmonic tapes with nanohole and nanoparticle arrays for refractometric and strain sensing, ACS Appl. Nano Mater. 3 (2020) 8242–8824.
[19] W.C. Chen, J.H. Shiao, T.L. Tsai, D.H. Jiang, L.C. Chen, C.H. Chang, B.H. Lin, J. H. Lin, C.C. Kuo, Multiple scattering from electrospun nanofibers with embedded silver nanoparticles of tunable shape for random lasers and white-light-emitting diodes, ACS Appl. Mater. Interfaces 12 (2020) 2783–2792.
[20] L. Dai, X. Lu, L. Song, Y. Huang, B. Liu, L. Zhang, J. Zhang, S. Wu, T. Chen, Macroscopic-oriented gold Nanorods in polyvinyl alcohol films for polarization-dependent multicolor displays, Adv. Mater. Interfaces 5 (2018) 1800026.
[21] T.G. Yun, M. Park, D.H. Kim, D. Kim, J.Y. Cheong, J.G. Bae, S.M. Han, I.D. Kim, All-transparent stretchable electrochromic supercapacitor wearable patch device, ACS Nano 13 (2019) 3141–3150.
[22] J. Li, H. Yan, X. Tan, Z. Lu, H. Han, Cauliflower-inspired 3D SERS substrate for multiple mycotoxins detection, Anal. Chem. 91 (2019) 3885–3892.
[23] K. Yang, S. Zong, Y. Zhang, Z. Qian, Y. Liu, K. Zhu, L. Li, N. Li, Z. Wang, Y. Cui, Array-assisted SERS microfluidic chips for highly sensitive and multiplex gas sensing, ACS Appl. Mater. Interfaces 12 (2020) 1395–1403.
[24] Z. Liu, H. Wang, P. Huang, J. Huang, Y. Zhang, Y. Wang, M. Yu, S. Chen, D. Qi, T. Wang, Y. Jiang, G. Chen, G. Hu, W. Li, J. Yu, Y. Luo, X.J. Loh, B. Liedberg, G. Li, X. Chen, Highly stable and stretchable conductive films through thermal-radiation-assisted metal encapsulation, Adv. Mater. 31 (2019), e1901360.
[25] S. Choi, S.I. Han, D. Jung, H.J. Hwang, C. Lim, S. Bae, O.K. Park, C.M. Tschabrunn, M. Lee, S.Y. Bae, J.W. Yu, J.H. Ryu, S.W. Lee, K. Park, P.M. Kang, W.B. Lee, R. Nezafat, T. Hyeon, D.H. Kim, Highly conductive, stretchable and biocompatible ag-au Core-sheath nanowire composite for wearable and implantable bioelectronics, Nat. Nanotechnol. 13 (2018) 1048–1056.
[26] S. Scarano, C. Berlangieri, E. Carretti, L. Dei, M. Minunni, Tunable growth of gold nanostructures at a PDMS surface to obtain plasmon rulers with enhanced optical features, Microchim. Acta 184 (2017) 3093–3102.
[27] Q. Zhang, J.-J. Xu, Y. Liu, H.-Y. Chen, In-situ synthesis of poly(dimethylsiloxane)–gold nanoparticles composite films and its application in microfluidic systems, Lab Chip 8 (2008) 352–357.
[28] M.L. Coluccio, G. Das, F. Mecarini, F. Gentile, A. Pujia, L. Bava, R. Tallerico, P. Candeloro, C. Liberale, F. De Angelis, E. Di Fabrizio, Silver-based surface enhanced Raman scattering (SERS) substrate fabrication using nanolithography and site selective electroless deposition, Microelectron. Eng. 86 (2009) 1085–1088.
[29] M. Iatalese, M.L. Coluccio, V. Onesto, F. Amato, E. Di Fabrizio, F. Gentile, Relating the rate of growth of metal nanoparticles to cluster size distribution in electroless deposition, Nanoscale Adv. 1 (2019) 228–240.
[30] M.L. Coluccio, F. Gentile, M. Francardi, G. Perozziello, N. Malara, P. Candeloro, E. Di Fabrizio, Electroless deposition and nanolithography can control the formation of materials at the Nano-scale for Plasmonic applications, Sensors 14 (2014) 6056–6083.
[31] V. Onesto, L. Cancedda, M. Coluccio, M. Nanni, M. Pesce, N. Malara, M. Cesarelli, E.D. Fabrizio, F. Amato, F. Gentile, Nano-topography enhances communication in neural cells networks, Sci. Rep. 7 (2017) 1–13.
[32] S.-H. Sunwoo, S.I. Han, H. Joo, G.D. Cha, D. Kim, S.H. Choi, T. Hyeon, D.-H. Kim, Advances in soft bioelectronics for brain research and clinical neuroengineering, Matter 4 (2020) 1923–1947.
[33] L. Bruno, S. Canto, L. Luciani, Localized heat treatment to improve the formability of steel pipes for hydraulic applications: process design and mechanical characterization, Int. J. Adv. Manuf. Technol. 119 (2022) 927–940.
[34] A.D. Rakic, A.B. Djurisic, J.M. Elazar, M.L. Majewski, Optical properties of metallic films for vertical-cavity optoelectronic devices, Appl. Opt. 37 (1998) 5271–5283.
[35] D.T. Pierce, W.E. Spicer, Electronic structure of amorphous Si from photoemission and optical studies, Phys. Rev. B 5 (1972) 3017.
[36] C.F. Guimarães, L. Gasperini, A.P. Marques, R.L. Reis, The stiffness of living tissues and its implications for tissue engineering, Nat. Rev. Mater. 5 (2020) 351–370.
[37] A.M. Handorf, Y. Zhou, M.A. Halanski, W.-J. Li, Tissue Stiffness Dictates Development, Homeostasis, and Disease Progression, Organogenesis 11, 2015, pp. 1–15.
[38] S.H.D.P. Lacerda, J.J. Park, C. Meuse, D. Pristinski, M.L. Becker, A. Karim, J. F. Douglas, Interaction of gold nanoparticles with common human blood proteins, ACS Nano 4 (2010) 365–379.
[39] P. Wang, X. Wang, L. Wang, X. Hou, W. Liu, C. Chen, Interaction of gold nanoparticles with proteins and cells, Sci. Technol. Adv. Mater. 16 (2015), 034610.
[40] D.V. Sotnikov, I.V. Safenkova, A.V. Zherdev, V.G. Avdienko, I.V. Kozlova, S. S. Babayan, V.Y. Gergert, B.B. Dzantiev, A mechanism of gold nanoparticle aggregation by immunoglobulin G preparation, Appl. Sci. 10 (2020) 475.
[41] M.L. Coluccio, F. Gentile, G. Das, A. Nicastri, A.M. Perri, P. Candeloro, G. Perozziello, R.P. Zaccaria, J.S.T. Gongora, S. Alrasheed, A. Fratalocchi, T. Limongi, G. Cuda, E. Di Fabrizio, Detection of single amino acid mutation in human breast cancer by disordered plasmonic self-similar chain, Sci. Adv. 1 (2015), e1500487.